Tectonophysics 726 (2018) 137–146

Contents lists available at ScienceDirect

Tectonophysics

journal homepage: www.elsevier.com/locate/tecto

Numerical investigation of deep-crust behavior under lithospheric extension

Megan Korchinski[a,*], Patrice F. Rey[b], Luke Mondy[b], Christian Teyssier[a], Donna L. Whitney[a]

[a] Department of Earth Sciences, University of Minnesota, Minneapolis, MN, USA
[b] EarthByte, School of Geosciences, University of Sydney, Sydney, Australia

ARTICLE INFO

Keywords:
Gneiss domes
Exhumation
Extension
Numerical modeling
Rheology

ABSTRACT

What are the conditions under which lithospheric extension drives exhumation of the deep orogenic crust during the formation of gneiss domes? The mechanical link between extension of shallow crust and flow of deep crust is investigated using two-dimensional numerical experiments of lithospheric extension in which the crust is 60 km thick and the deep-crust viscosity and density parameter space is explored. Results indicate that the style of extension of the shallow crust and the path, magnitude, and rate of flow of deep crust are dynamically linked through the deep-crust viscosity, with density playing an important role in experiments with a high-viscosity deep crust. Three main groups of domes are defined based on their mechanisms of exhumation across the viscosity-density parameter space. In the first group (low-viscosity, low-density deep crust), domes develop by lateral and upward flow of the deep crust at km m.y^{-1} velocity rates (i.e. rate of experiment boundary extension). In this case, extension in the shallow crust is localized on a single interface, and the deep crust traverses the entire thickness of the crust to the Earth's near-surface in 5 m.y. This high exhuming power relies on the dynamic feedback between the flow of deep crust and the localization of extension in the shallow crust. The second group (intermediate-viscosity, low-density deep crust) has less exhuming power because the stronger deep crust flows less readily and instead accommodates more uniform extension, which imparts distributed extension to the shallow crust. The third group represents the upper limits of viscosity and density for the deep crust; in this case the low buoyancy of the deep crust results in localized thinning of the crust with large upward motion of the Moho and lithosphere-asthenosphere boundary. These numerical experiments test the exhuming power of the deep crust in the formation of extensional gneiss domes.

1. Introduction

Flow of the deep crust is a significant mechanism for the transport of heat and mass during orogeny and is a critical geodynamic process in the chemical and physical evolution of continents. Horizontal flow is one mode of orogenic collapse (Rey et al., 2001) and may contribute to the growth of orogenic plateaus (e.g., Clark and Royden, 2000). Vertical flow in combination with horizontal flow can bring hot, deeply-sourced material to shallower levels (e.g., Burg et al., 2004; Schulmann et al., 2008; Rey et al., 2011; Teyssier and Whitney, 2002), in some cases traversing most of the thickness of the orogenic crust (Whitney et al., 2015) to within a few kilometers of the Earth's surface (Stübner et al., 2013a, 2013b; Toraman et al., 2014).

Vertical flow of hot, deep crust can create crustal-scale structures that are characterized by domal patterns of foliation in high-grade metamorphic rocks. These gneiss domes are exposed in most orogens, from Archean to Cenozoic (Teyssier and Whitney, 2002; Whitney et al., 2004, 2013). Domes are typically cored by migmatite and associated granite, which represent crystallized partial melt and magma, respectively. In many gneiss domes, the P-T paths obtained from layers and lenses of refractory lithologies included in the host quartzofeldspathic gneiss indicate isothermal decompression that was equivalent to at least 10–20 km of exhumation at high temperature (e.g., Augier et al., 2005; Bonev et al., 2005; Caby et al., 2001; de Sigoyer et al., 2004; François et al., 2014; Norlander et al., 2002; Whitney et al., 2004).

Dome formation has been previously investigated in 2D and 3D numerical modeling studies, wherein initial and/or boundary conditions were varied. Parameters varied in models include: (a) the rheology of the crust (e.g. Buck, 1991); (b) the initial geotherm (e.g. Tirel et al., 2004a; Tirel et al., 2008; Wijns et al., 2005); (c) the presence of temperature anomalies in the deep crust (e.g. Burov et al., 2014; Koptev et al., 2017); (d) the presence of partial melt in the deep crust (e.g. Rey et al., 2011; Rey et al., 2009a, 2009b; Schenker et al., 2012); (e) the presence of inherited rheological layers within the crust (e.g. Fayon et al., 2004; Huet et al., 2011; Labrousse et al., 2016; Le Pourhiet et al., 2012; Schenker et al., 2012); (f) the strength and/or presence of

* Corresponding author.
E-mail address: korch009@umn.edu (M. Korchinski).

https://doi.org/10.1016/j.tecto.2017.12.029
Received 9 May 2017; Received in revised form 27 December 2017; Accepted 29 December 2017
Available online 08 February 2018
0040-1951/

an initial weak zone in the crust (e.g. Fayon et al., 2004; Mezri et al., 2015); and (g) the imposed extensional velocity (e.g. Buck, 1991; Rey et al., 2011; Rey et al., 2009a, 2009b; Schenker et al., 2012; Tirel et al., 2004b; Tirel et al., 2008). We present a systematic exploration of the independent impact of the density and viscosity of the deep crust on (1) the mechanical links between the deep and shallow crust during extension, and (2) the conditions and mechanisms of deep-crust exhumation in extensional domes.

This study executed a series of 2D numerical experiments of lithospheric extension in which the viscosity and density of the deep crust were varied systematically. In order to capture the first order relationship between viscosity, strain rate and stress, we utilize a flow law that is representative of the crust to build a framework that can be used to explore the impact of compositional variances observed in nature. We used two starting crustal thicknesses (40 and 60 km), and two extensional velocities, 2 cm yr^{-1} (fast) and 2 mm yr^{-1} (slow), to evaluate the interplay among buoyancy, viscosity, and extension velocities during dome development. Numerical experiments reveal the parameter combinations that favor or suppress the generation of extensional gneiss domes, and demonstrate how the flow of deep crust is dynamically linked to strain localization or distribution in the shallow crust and the mantle.

2. Numerical experiment design

We use *Underworld*, a particle-in-cell finite element code that solves the equations for momentum, energy, and mass for incompressible flow of low Reynolds numbers (Moresi et al., 2007; Moresi et al., 2003) (Appendix A). Experiments are run using the Lithospheric Modelling Recipe: (https://github.com/OlympusMonds/lithospheric_modelling_recipe), a Python wrapper that facilitates efficient experiment design and execution. The reference experiment maps a 360 km long and 160 km deep model over a computational grid with 1 km resolution (Fig. 1). Models include from top to bottom: 10 km air layer, 20 km shallow crust (2620 $kg{\cdot}m^{-3}$), 40 km deep crust (2700–3100 $kg{\cdot}m^{-3}$), 40 km lithospheric mantle (3370 $kg{\cdot}m^{-3}$), and 50 km asthenosphere (3395 $kg{\cdot}m^{-3}$) (Fig. 1).

In the shallow crust, a 2 km-thick prism made of weaker material acts as a fault (45° dip) (Fig. 1). The fault forces deformation to localize in the center of the numerical experiment. This facilitates comparison of flow and strain patterns among the different experiments, and mitigates boundary effects (e.g., asymmetric flow) that would occur when a dome develops close to a vertical wall in the model. Similar experiments conducted by Rey et al. (2009b) tested the effect of a dipping weak prism versus a point weakness to force strain localization in the center of the experimental domain and found negligible differences. The dipping heterogeneity is preferred because it provides a geologically realistic asymmetry in the structural development of the dome (Rey et al., 2009b).

Material viscosities are temperature and strain-rate dependent, and plastic rheologies include a strain-weakening function. The visco-plastic rheology of the shallow crust is based on quartzite (Paterson and Luan, 1990), and the visco-plastic rheology of the lithospheric mantle and asthenosphere is based on wet olivine (Fig. 1; Appendix A) (Hirth and Kohlstedt, 2004). The deep crust has visco-plastic rheology based on the dry mafic granulite model of Wang et al. (2012); the starting viscosity of this layer is varied within the experiment suite.

A swarm of circular passive markers gives a qualitative representation of the finite strain field within the deep crust (Rey et al., 2009a). These markers were initially distributed as regularly spaced circles, allowing the evolution of finite strain orientations and strain intensity to be tracked within each experiment, and to be compared, at least qualitatively, across the suite of experiments. Recent 3D experiments (Rey et al., 2017) utilize similar strain markers to track finite strain in domes that develop in pull-apart systems. These 3D models show that dome material displays a double dome of foliation and a strong lineation parallel to the axis of the dome, which cannot be revealed by 2D models (see also Le Pourhiet et al., 2012). However, 2D models produce flow fields that are similar to the flow fields observed in the cross section projection of 3D models, as well as similar flow velocities, exhumation velocities, and thermal structure. Therefore, the computationally economical models presented here, although they limit strain within 2D, are nevertheless helpful for comparing flow fields within the deep crust across a wide spectrum of parameters.

The initial thermal state of each experiment is calculated using a period of thermal evolution under null extension, crustal radiogenic heating, basal heat flow, and constant surface temperature (Table 1; Appendix A). The resulting initial geotherm is characterized by a Moho temperature of ~850 °C (Fig. 1; Appendix A).

The starting reference density of deep crust is varied systematically from 2700 to 3100 $kg{\cdot}m^{-3}$ by increment of 100 $kg{\cdot}m^{-3}$. Within each experiment, density depends on temperature and melt fraction when present (see below); the coefficient of thermal expansion is kept constant across all experiments.

The reference viscosity of the deep crust is also systematically varied by changing the pre-exponential factor (A; $\eta = \frac{1}{2}\cdot A^{-1/n}\cdot\exp\left[\frac{Q}{n\cdot R\cdot T}\right]\cdot\varepsilon^{(1-n)/n}$; Appendix A) (Rey et al., 2009b, 2011). The reference viscosities are hereafter referred to as *weak* (1.0E19 Pa·s), *intermediate* (1.0E20 Pa·s), and *strong* (1.0E21 Pa·s). These values describe the viscosity at the base of the crust (immediately above Moho) at the initial time step.

The presence of melt in a dome facilitates the upward advection of heat and material (Rey et al., 2009b). In order to account for the mechanical and thermal effects of partial melting, a heuristic function is included (Rey et al., 2009a, 2009b). The melt fraction is a function of the supersolidus temperature (McKenzie and Bickle, 1988) (Appendix A). The solidus and liquidus for the crust and mantle are both temperature- and pressure-dependent and are described by polynomial functions (Fig. 1); a partial melt layer exists at the start of experiments where the geotherm crosses the solidus. The maximum partial melt fraction is 0.3, which is in line with melt fractions inferred in many gneiss (migmatite) domes (Whitney et al., 2004). The reference density of the crust decreases linearly to a maximum of 13% (Clemens and Droop, 1998), and material viscosity decreases linearly by three orders

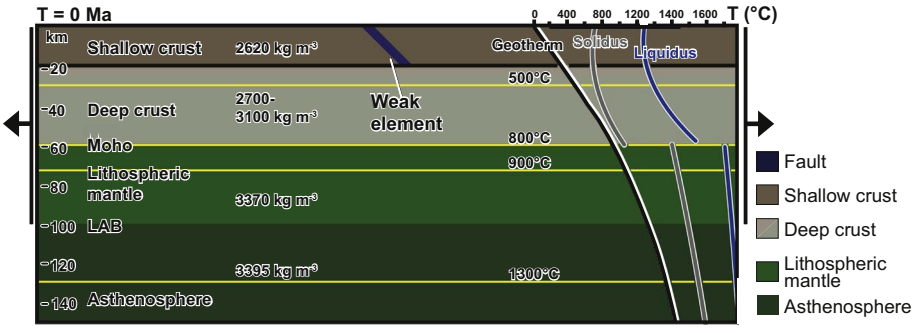

Fig. 1. Experiment input parameters, boundary conditions, and geometry. Yellow lines delineate the initial depth of isotherms. The weak element (i.e. detachment fault) is 2 km wide and is outlined in blue. The fault has the same density of the shallow crust and a Newtonian viscosity (1.0E19 Pa·s). Black arrows show applied extension velocity. LAB: lithosphere-asthenosphere boundary. (For interpretation of the references to color in this figure legend, the reader is referred to the web version of this article.)

Table 1
Rheological parameters.

Parameter	Shallow crust	Deep crust	Lithosph. mantle	Asthenosph. mantle
Reference temperature (K)	293			
Dislocation creep viscous rheology	Wet quartzite[a]	Dry mafic granulite[b]	Wet olivine[c]	Wet olivine[c]
Reference density ($kg{\cdot}m^{-3}$)	2620	2700–3100	3370	3395
Heat capacity ($J\,K^{-1}\,kg^{-1}$)	1000			
Thermal diffusivity ($m^2\,s^{-1}$)	1.0E − 6			
Latent heat of fusion ($kJ\,kg^{-1}$)	300			
Radiogenic heat production ($W\,m^{-3}$)[d]	0.7E − 6	0.4E − 6	0.02E − 6	0.02E − 6
Melt fraction density change ($M_{\Delta\rho f}$)[e]	0.13			
Solidus term 1 (K)	993	993	1393.661	1393.661
Solidus term 2 ($K\,Pa^{-1}$)	− 1.2E7	− 1.2E7	1.32899E − 7	1.32899E − 7
Solidus term 3 ($K\,Pa^{-2}$)	1.2E16	1.2E16	− 5.104E − 18	− 5.104E − 18
Liquidus term 1 (K)	1493	1493	2013	2013
Liquidus term 2 ($K\,Pa^{-1}$)	− 1.2E7	− 1.2E7	6.15E − 8	6.15E − 8
Liquidus term 3 ($K\,Pa^{-2}$)	1.6E16	1.6E16	3.12E − 18	3.12E − 18
Friction coefficient	0.577			
Softened friction coefficient	0.1154			
Softened cohesion (MPa)	2	4	2	2
Pre-exponential factor ($MPa^{-n}\,s^{-1}$)	6.60692E − 8	10E − 2	1600	1600
Stress exponent	3.1	2.8–3.6	3.5	3.5
Activation energy ($kJ\,mol^{-1}$)	135	244	520	520
Activation volume ($m^3\,mol^{-1}$)	0	0	23E − 6	23E − 6
Water fugacity	0	0	1000	1000
Water fugacity exponent[f]	0	0	1.2	1.2
Melt viscous softening factor	1.0E − 3	1.0E − 3	1.0E − 2	1.0E − 2
Viscous softening melt fraction	0.2–0.3	0.2–0.3	0.03–0.08	0.03–0.08

[a] Parameters were derived from Paterson and Luan (1990).
[b] Parameters were derived from Wang et al. (2012).
[c] Parameters were derived from Hirth and Kohlstedt (2004).
[d] Parameters were derived from Hasterok and Chapman (2011).
[e] Melt and other parameters were derived from Rey and Muller (2010).
[f] A zero value denotes that this effect on the viscous flow law is incorporated into the pre-exponential factor.

of magnitude across a critical melt fraction range between 0.2 and 0.3. Previous numerical experiments of the development of extension-driven domes have shown that the melt fraction increases to its maximum value over a few kilometers as the solidus is translated upward through the deep crust (Rey et al., 2009b). Therefore, numerical experiments are not significantly impacted by decreasing the critical melt fraction to lower values (i.e. 2–12%) (Rey et al., 2009b; Rosenberg and Handy, 2005). Melt does not segregate from the host rock in the experiments; this *en masse* movement of partially molten material is consistent with observations of migmatite-cored metamorphic core complexes in which only a relatively small volume of leucogranite is extracted from the partial melt layer (Teyssier and Whitney, 2002).

Experiments are run at two extension velocities: 2.0 and 0.2 cm yr^{-1}. The velocity boundary conditions are applied to the vertical walls down to the base of the lithosphere (Fig. 1). A function at the base of the model allows inflow of asthenosphere to isostatically balance the extension-related outward flow of material at the sides.

3. Experimental results

The experiments systematically explore flow and deformation within the lithosphere as a function of the density and viscosity of the deep crust. Selected experiment outputs are presented as two main suites: *fast* extension (2 cm yr^{-1}; Fig. 2a) and *slow* extension (0.2 cm yr^{-1}; Fig. 2b). We describe first-order results across the parameter space, and then focus on how the flow of deep crust varies across the experiment suite, noting the strain and kinematic patterns that describe the flow. We present and compare experimental results after 5 m.y. for fast extension and 50 m.y. for slow extension, corresponding to 28% extension. Appendix B presents the fast and slow experiment suites experimental results at 39% and 55% extension (unless otherwise noted in Appendix B), as well as the effective viscosity and strain rate of the fast and slow experiment suites at 28%, 39%, and 55% extension.

3.1. Exhumation of deep crust and strain localization in shallow crust

3.1.1. Fast extension

Crustal-scale vertical transport of deeply sourced crustal material to the near-surface occurred across the entire experiment suite (Fig. 2a). Experimental results show that the magnitude of exhumation of deep material is primarily dependent on the ability of deformation to localize in the shallow crust. In experiments with a weak deep crust (Fig. 2a_3), strong localization of strain on the initial weak element results in boudinage of the shallow crust, which creates space and allows rapid upward flow of deep, low-viscosity material into a broad (up to 100 km wide) core complex. Crust that was partially molten at the start of the experiment remains partially molten to depths < 15 km, while temperature remains within 100 °C of the maximum temperature (T_{max}) at peak pressure.

In experiments with a strong or intermediate deep crust (Fig. 2$a_{1–2}$), the mechanical coupling between the shallow crust and the deep crust is stronger, and localization of deformation in the shallow crust is less efficient. Strain initially localizes along the original normal fault and newly formed conjugate faults (Fig. 2a_1) before migrating > 30 km away from the imposed weak element (Fig. 2a_1).

Vertical flow within the dome is markedly different across experiments with differing deep crustal viscosities. Material sourced from a weak deep crust is transported vertically up to 5 km of the Earth's surface after 5 m.y. (28% extension; Fig. 2a_3). In experiments with an intermediate and strong deep crust, rocks from the deep crust are transported up to 20 km of the Earth's surface at 28% extension, resulting in significantly less exhumation than in the weak experiments.

The magnitude of exhumation is less dependent on the density of the deep crust (Fig. 2a). For example, for weak deep crust at 28% extension, the difference in total vertical transport (Δz) between experiments with a low density deep crust and high density deep crust is only ~4 km (Fig. 2a_3). This is an order of magnitude lower than the variation of vertical transport achieved across experiments by contrasting

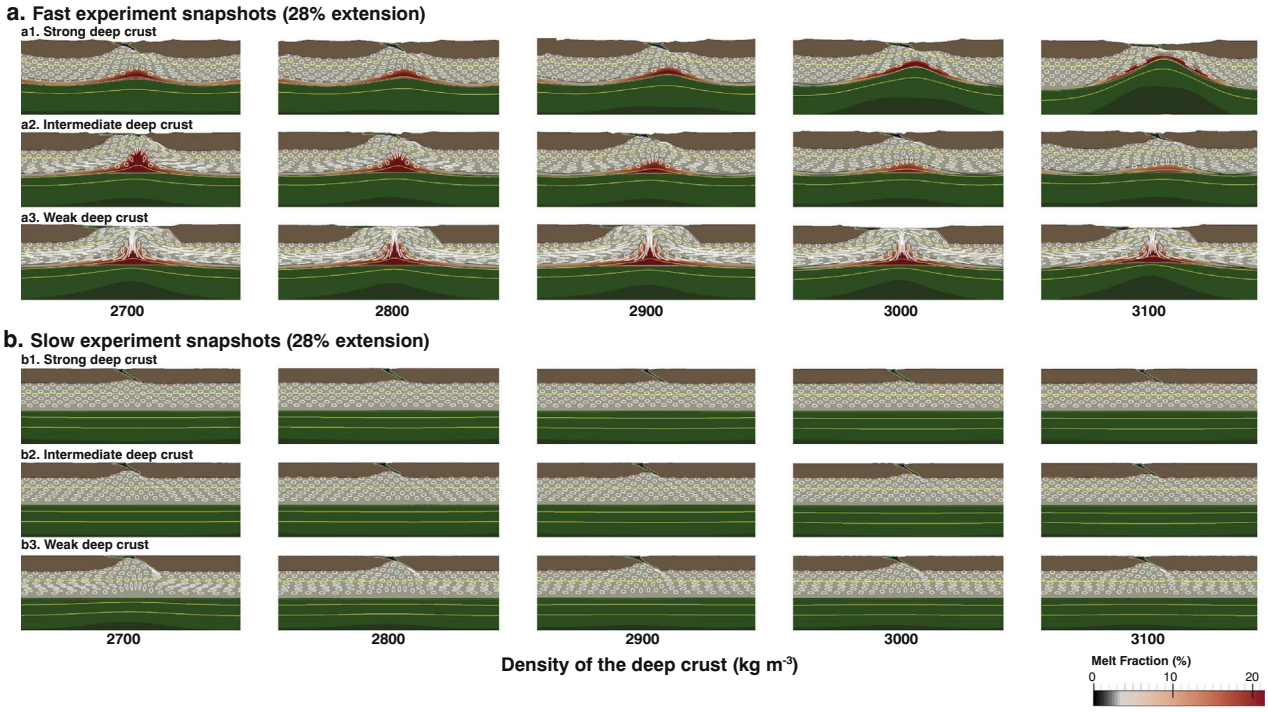

Fig. 2. Experimental snapshots illustrating crustal geometry and strain patterns in the deep crust. (a) Fast extension experiments (2 cm yr^{-1}). Strain ellipses are shown in white within the deep crust. These markers start out as circles, and become deformed as the experiment proceeds thereby recording the intensity and direction of strain. Note that the melt fraction in the deep crust is shown as a red shading. (b) Slow extension experiments (0.2 cm yr^{-1}). Complete experimental results are presented in Appendix B. (For interpretation of the references to color in this figure legend, the reader is referred to the web version of this article.)

deep crustal viscosities.

3.1.2. Slow extension

Vertical transport of deeply sourced rocks is minimal in the slow-extension experiment suite, regardless of the physical parameters used for the deep crust (Fig. 2b). Localization of strain occurs on a single fault in the weak, low-density experiments, but it is significantly less than the localization that occurs in experiments with fast extension. Decompression melting of the deep crust occurs in the weak, low-density experiments; however, the predicted melt fraction in these experiments is negligible relative to that present in the equivalent fast-extension experiment (Fig. 2b; Fig. B1.7–B1.9, Appendix B).

3.2. Deep crust strain patterns

The passive markers inserted in the deep crust record the various strain patterns that develop across the parameter space, and can be compared to foliation trajectories within and around natural domes.

3.2.1. Fast extension

At one end of the viscosity-density parameter space (weak deep crust, 2700 $kg{\cdot}m^{-3}$) strain markers highlight the partitioning of strain across a décollement channel in the deep crust (Fig. $2a_3$). The lowest viscosity deep crust flows horizontally inward, toward the zone of extension, while the upper layer of deep crust moves away from the center of the experiment, consistent with the imposed extension boundary conditions. The inward flow in the low-viscosity channel is bounded above and below by sub-horizontal high-strain zones with opposite senses of shear. Inward flow of the deep crust is nearly symmetrical about the center of the experiment and results in the viscous collision of material directly below the zone of shallow crust thinning. This collision leads to the development of a vertical high-strain zone (horizontal contraction) between two subdomes of foliation ('double dome'; Gessner et al., 2007; Labrousse et al., 2016; Rey et al., 2011; Schenker et al., 2012). Substantial upward flow is accommodated within the subdomes resulting in considerable exhumation of the deep crust. As the deep crust reaches shallow depths (< 10 km), flow transitions from dominantly vertical to dominantly horizontal and outward, away from the dome core (Fig. $2a_3$).

In the parameter space, the double dome geometry is best exemplified in the weak, low-density experiment, and the main features of this geometry (double dome, vertical high-strain zone) persist across all investigated densities from 2700 to 3100 $kg{\cdot}m^{-3}$ (Fig. $2a_3$). The double dome geometry is also present in the intermediate viscosity experiments (Fig. $2a_2$), particularly for low densities (2700 and 2800 $kg{\cdot}m^{-3}$). Increasing density suppresses the upward flow of deep crust and limits the development of double domes. Nevertheless, vertical foliation still develops directly below the zone of upper crust thinning (center of experiment) in the higher density, intermediate viscosity deep crust cases (Fig. $2a_2$), indicating some degree of deep crust inward flow and viscous collision during extension.

In the case of strong deep crust (Fig. $2a_1$), no pronounced inward flow develops in the deep crust. The strain ellipses reveal uniform thinning with a zone of localized necking in the center of the experiment, creating substantial relief of both the Moho and the lithosphere-asthenosphere boundary (LAB). Necking is amplified when the density increases from 2700 to 3100 $kg{\cdot}m^{-3}$ (Fig. $2a_1$). The substantial exhumation of strong deep crust in experiments with a high density deep crust (3100 $kg{\cdot}m^{-3}$; Fig. $2a_1$) is caused primarily by localized thinning of the crust (i.e. Moho depths of 15 km), indicating that high-viscosity, high-density thick crust could be rifted exposing deep crust and mantle sections at the surface.

3.2.2. Slow extension

Strain ellipses show that the deep crust undergoes uniform strain (Fig. 2b). Extension of the lithosphere results in overall vertical shortening and horizontal lengthening of deep crust material (Fig. B1.7–B1.9, Appendix B). The exceptions to this pattern are the weak, low-density experiments in which up to 5 km of upward flow of deep crust material (over 5 m.y. experiment duration) is present as a result of

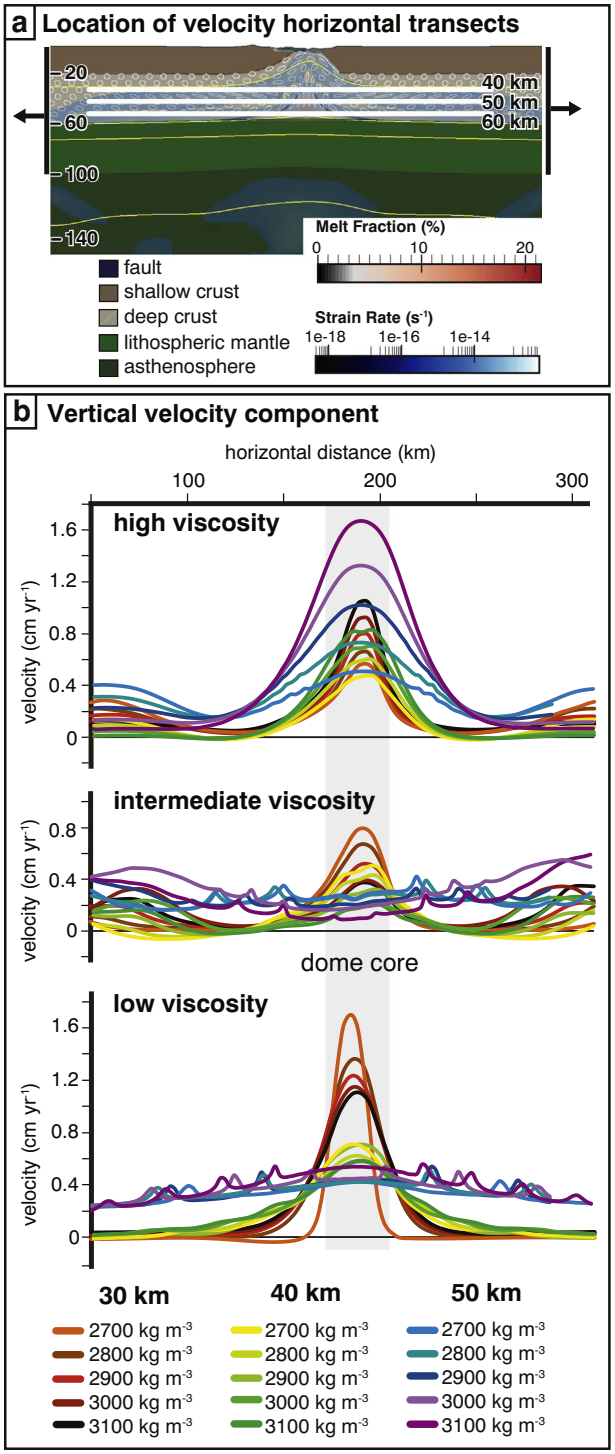

Fig. 3. Vertical component of the velocity field along three horizontal profiles. (a) Velocity profiles at 30, 40 and 50 km depth located in the low viscosity, low density (2700 kg·m^{-3}) experiment. Velocity profiles were extracted at 11% extension (2 m.y. experiment time; 2 cm yr^{-1} extension rate). (b) Profiles of the vertical component of velocity for various deep crust viscosity and densities. The approximate location of the dome core shown in grey.

boudinage of the shallow crust (Fig. B1.7, Appendix B). In this case, strain ellipses in the core of the dome initially track horizontal shortening, followed by vertical shortening caused by bulk lithospheric extension (Fig. B1.7, Appendix B). This evolution represents the initiation and subsequent suppression of a double dome (Fig. 2b$_3$).

The upward motion of the Moho and LAB is the result of uniform crustal thinning in the slow experiment suite, with no significant Moho and LAB relief (Figs. 2b; B1.7–B1.9, Appendix B). A slight upward deflection of the Moho and LAB exists at the sides of experiments in the case of high-density, intermediate-strong deep crust.

4. Horizontal and vertical flow of deep crust

The results of the numerical experiments provide information about the flow field across the experimental parameter space, including the magnitude of horizontal and vertical flow components, the latter being critical to the assessment of the exhuming power of domes. In this section, we focus on the fast experiment suite, in which horizontal and vertical flow varies significantly. For all values of viscosity and density, we take a snapshot of the magnitude, distribution, and velocity of horizontal and vertical flow at 2 m.y. (11% extension; Fig. 3, 4).

4.1. Vertical flow

Vertical component of velocity, evaluated across the experiment at depths of 30, 40, and 50 km (Fig. 3), shows that exhumation dynamics varies significantly as a function of depth and viscosity. In the dome-core area, rapid exhumation is achieved for all combination of densities and viscosities; however the maximum flow varies horizontally (Fig. 3b). Results show that weak deep crust achieve exhumation velocity approaching the driving extension velocity (1.7 cm yr^{-1}, Fig. 3b). However, peak vertical velocity varies considerably for different viscosity-density scenarios and also varies across each experiment for different sites relative to the shallow-crust localizing element (fault) and the underlying dome-core that develops. Interestingly, two exhumation modes emerge: (1) exhumation of the deep crust occurs without development of significant relief on the Moho (e.g., 2a$_3$), and (2) exhumation of the deep crust is coeval with substantial (~40 km) exhumation of the Moho and little flow of the deep crust (Fig. 2a$_1$, 3100 kg·m^{-3}).

4.2. Horizontal flow

During lithospheric extension, the magnitude of horizontal flow in the deep crust is primarily dependent on its viscosity, and to a less extend to its density (Fig. 4). The horizontal component of the velocity field (positive when particles move to the right) varies from the value of the driving extensional velocity in the rigid parts of the lithosphere, to opposite but similar values in low-viscosity and low-density experiments (Fig. 4b profiles at 30 km). Experiments with high-viscosity and high-density deep crust, however, experience little flow as deformation is dominated by upwards translation of the deep crust (Fig. 4b). Closer to the experiment center, intermediate- and low-viscosity deep crust experiences strong convergent flow towards the developing 'dome'.

5. Exhumation of deep crust

The 2D experimental suite provides insight into the dynamics of gneiss domes that develop under extension. Exhumation of the deep crust in a domal structure occurs in the fast-extension suite of experiments and, to a lesser extent, under slow extension in the weak deep crust experiments.

In the fast-extension suite of experiments, domes are common (Fig. 2a). In many cases, the material that feeds the dome is deeply sourced and flows horizontally over tens of kilometers and flows vertically toward the surface. Under fast extension, the viscosity of the deep crust exerts the primary control on the amount of exhumation of deeply sourced material in the dome, on the strain patterns in the deep crust, and on whether deformation in the shallow crust is distributed or localized. The density of the deep crust has a minor influence in cases of low-viscosity deep crust but significantly influences the behavior of high-viscosity deep crust (Fig. 2a$_1$).

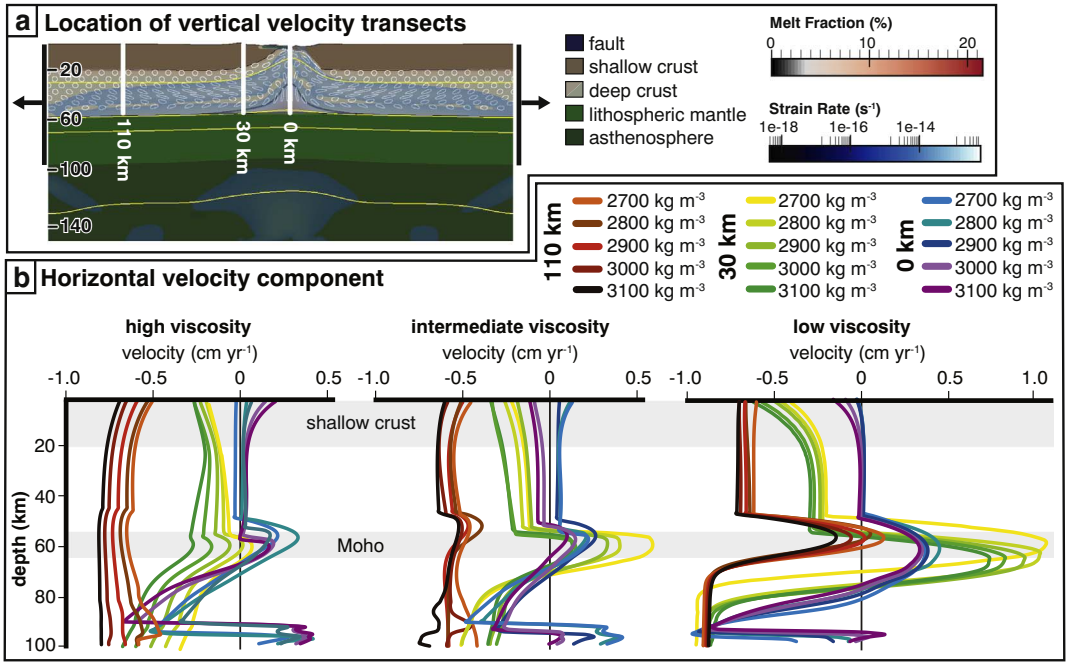

Fig. 4. Horizontal component of the velocity field along three vertical profiles. (a) Velocity profiles at 0, 30 and 110 km from the center of the model located in the low viscosity, low density (2700 kg·m^{-3}) experiment. Velocity profiles were extracted at 11% extension (2 m.y. experiment time; 2 cm yr^{-1} extension rate). (b) Profiles of the horizontal component of velocity for various deep crust viscosities and densities. The approximate location of the shallow crust, deep crust, and Moho are shown in grey.

Under slow extension, overall thinning of the lithosphere occurs across the entire parameter space (Fig. 2b; Appendix B). Using similar extension velocities, previous numerical studies have produced deep-crustal domes with as little as 13% extension (e.g. extension velocities < 0.6 cm yr^{-1}; Koptev et al., 2017; Mezri et al., 2015). However, as our experiments have no thermal anomaly within the deep crust (i.e. no addition-crustal heat source beyond the background radiogenic heat, and no mantle plume), the lithosphere undergoes thinning without significant faulting within the shallow crust and flow within the deep crust.

5.1. Exhumation modes and velocity

In this section, we explore different modes of exhumation and consider associated exhumation velocities and P-T paths during ascent of deep crust. Three modes of exhumation can be defined across the experiment parameter space (Figs. 2; 5). Mode A comprises cases where the exhumation of deep crust is the result of deep crustal flow with little relief developed on the Moho, extreme thinning of the shallow crust, and the formation of a double dome of foliation (Fig. 5a). Mode B also involves deep crustal flow; however the shallow crust thins uniformly relative to Mode A, and double dome development is limited (Fig. 6a). Mode C corresponds to the case where the deep crust and Moho are exhumed by lithosphere necking owing to the concentration of extension at the center of the model while the lithosphere away from the center undergoes negligible extension (Fig. 6a).

Let us consider a 50-km deep particle located at the center of the model domain, and trace its ascent for all viscosity/density pairs in the parameter space (Fig. 6). In the case of experiments with a weak deep crust, the exhumation velocity of the particle is on the order of 10 km m.y^{-1} and exhibits a slight acceleration with time; exhumation velocities are not dependent on the density of the deep crust. In the case of experiments with an intermediate deep crust, the exhumation velocity of the particle is on the order of 10 km m.y^{-1} in the first few million years, after which exhumation decelerates. This deceleration is positively correlated with the density of the deep crust. The particle remains below ~20 km depth at 28% extension, except in the case of lowest density deep crust where the particle reaches ~10 km depth. In the case of experiments with a strong deep crust, the particle is exhumed efficiently to within ~25 km from the surface for the low density deep crust and to ~15 km depth for the high density deep crust.

When exhumation velocities for 50 km deep particles are plotted in the density viscosity parameter space, Mode A corresponds to experiments where the exhumation of deep crust is rapid (6–13 km m.y^{-1}) (Fig. 6c). Mode B corresponds to experiments with exhumation velocities of ~5 km m.y^{-1}, and even though double domes do develop, an intermediate to high viscosity deep crust combine with the uniform thinning of shallow crust to suppress deep crust exhumation (Fig. 6a, c). Mode C is restricted to experiments with a high density (> 2900 kg·m^{-3}) and strong deep crust (Fig. 6c). Exhumation is initially isothermal for all three modes, from ~50 km to ~25 km (Fig. 6d). Modes A and B are easily distinguished as Mode B experiences slight cooling and remains at high temperatures and pressures for the initial 5 m.y., whereas Mode A deep crust reaches the near-surface and cools rapidly after 2 m.y. (Fig. 6d). Mode C also shows exhumation of the 50 km deep particle; however, the deep crust also remains at high temperatures and pressures for the initial 5 m.y.

In the case of Mode C, exhumation is achieved by necking of the crust and shearing of the mantle lithosphere; the switch in behavior from the low density to high density cases for the high-viscosity deep crust case merits further scrutiny. Why would denser crust exhume faster than less dense crust? If one considers the entire extent of each high-viscosity model (5 models) (Fig. 2a$_1$), one realizes that the lithosphere undergoes limited thinning away from the center of the experiment in the case of a high density deep crust (> 2900 kg·m^{-3}), which yields an increase in the stretching (B) factor at the center of the experiment (Fig. 7). Therefore, given that the experiment boundaries are pulled at the same velocity for all fast experiments, the thinning deficit in the overall lithosphere with dense deep crust is achieved in a more limited region in the center of the model, and therefore the velocity of exhumation is greatest when the deep crust is denser. This is made possible by the localization of conjugate normal shearing through the crust in the center of the experiment that is controlled by the initial model fault; the end result is efficient upward motion of the Moho and

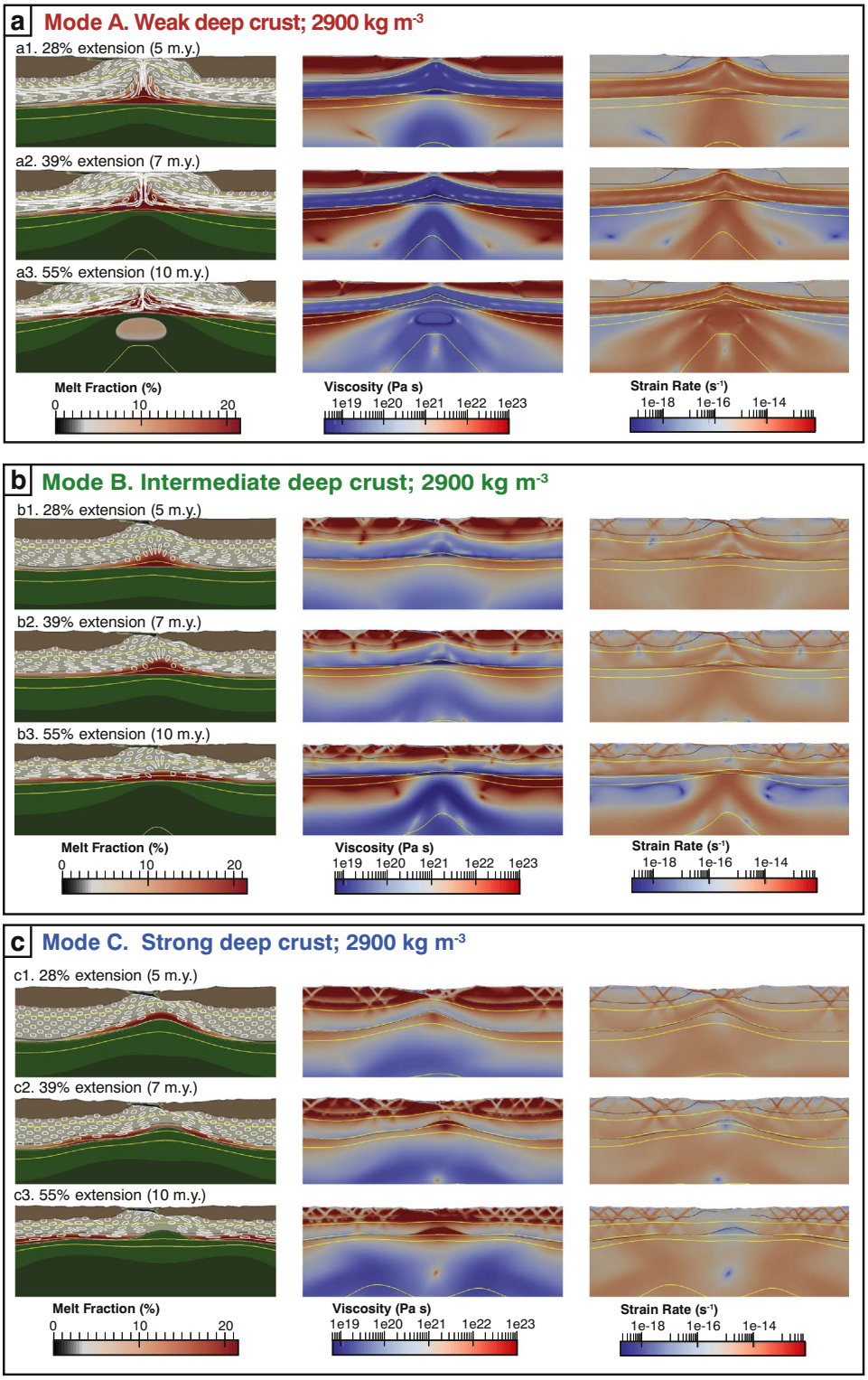

Fig. 5. Experiment snapshots, effective viscosity, and strain rate of Mode A (panel a), Mode B (panel b), and Mode C (panel c) exhumation mechanisms for the fast experiment suite. Results are presented for 28%, 39%, and 55% extension. Complete experimental results, along with effective viscosity and strain rate, for the fast and slow experiment suite are presented in Appendix B.

shearing of the underlying lithosphere. More generally, one can surmise that a dense, horizontally extensive deep crust favors lithospheric necking, especially if deformation is localized (pre-existing weakness) and rapid exhumation of the Moho and possibly the mantle.

5.2. Exhumation modes and mechanical coupling of deep and shallow crust

The degree to which shallow and deep crustal layers are mechanically coupled is key in producing Mode A or Mode B domes. In Mode A domes, the upper deep crust is mechanically coupled to the shallow crust, and partially decoupled from the lower deep crust across a

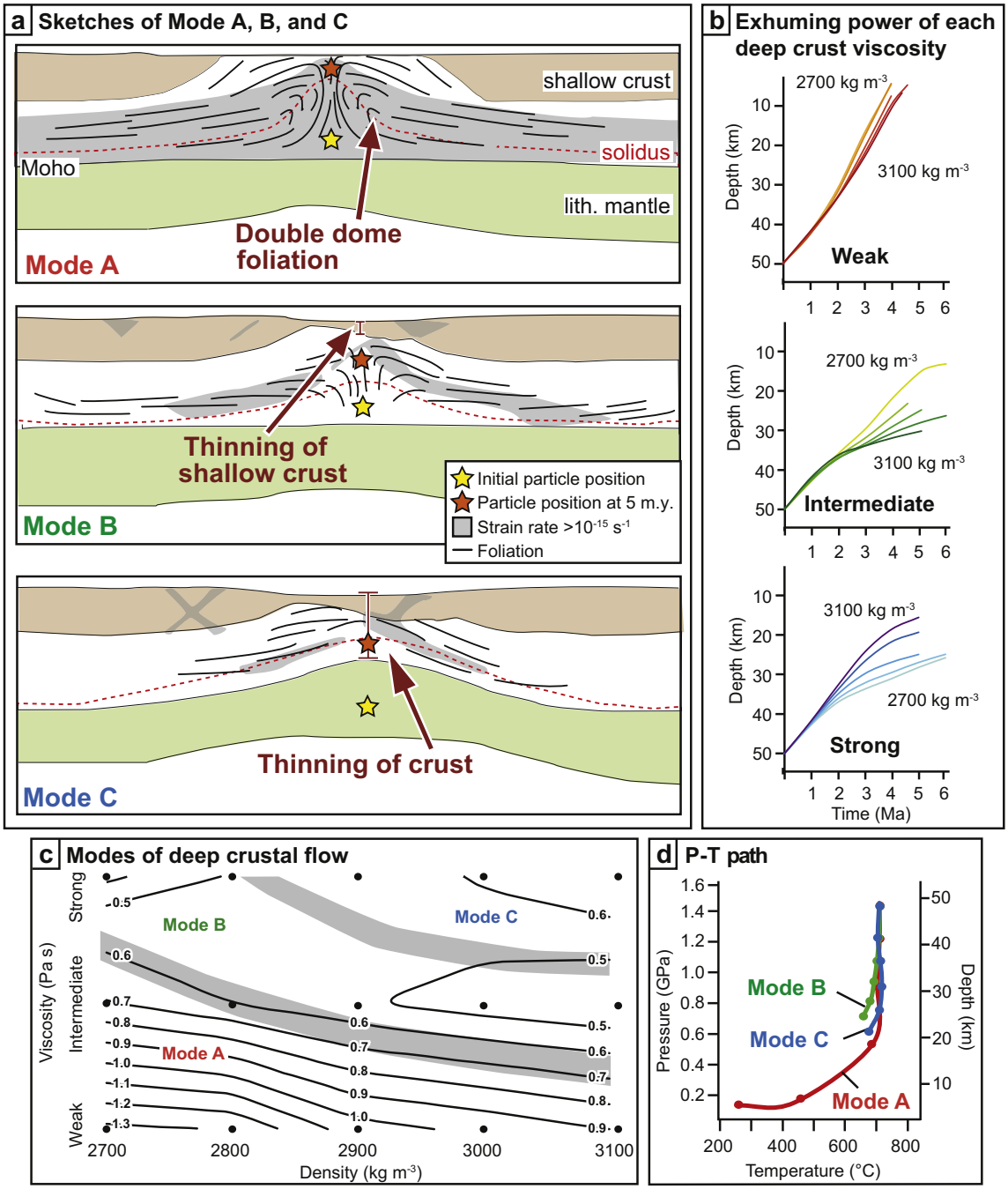

Fig. 6. (a) Sketches of mode A, B, and C exhumation mechanisms at 5 m.y. (28% extension). (b) dz/dt for various deep crust viscosities (fast experiment suite). Each set of curves is colored by density of the deep crust and shows the vertical path of the particle or passive tracer denoted in panel (a) as a yellow star. (c) Viscosity density parameter space contoured for the average exhumation velocity (cm yr^{-1}) over 5 m.y. of the particle shown in panel (a). See text for more information. (d) Pressure-temperature path for the particle shown in panel (a) for mode A, B, and C exhumation mechanism over the initial 5 m.y. (28% extension; 2 cm yr^{-1} extension rate). Each dot on P-T path represents 1 m.y. (For interpretation of the references to color in this figure legend, the reader is referred to the web version of this article.)

décollement (Fig. 5a). The normal fault breaks apart the shallow crust, and the lower deep crust undergoes vertical transport into space previously occupied by the shallow crust and the upper deep crust (Fig. 3, 4). The inward horizontal flow of the lower deep crust and the outward horizontal flow of the shallow crust/upper deep crust results in widespread high stain ($> 10^{-14}\ s^{-1}$) across the entire deep crust (Fig. 5a), with a mid-crustal shear zone characterized by high finite strain. By comparison, the Mode B deep crust exhibits high-viscosity, low strain-rate regions, each of which corresponds to a set of conjugate faults in the shallow crust (Fig. 5b). These regions represent mechanical coupling between the shallow crust and the deep crust, which reduces the horizontal and vertical flow of the deep crust in Mode B compared to Mode A domes (Fig. 4c), and thins the shallow crust without breaking it apart completely (Fig. 6a).

5.3. *Insights from numerical experiments on convergent deep-crustal flow in extensional gneiss domes*

The horizontal and vertical flow of the deep crust in experiments that yield Mode A and B exhumation mechanisms creates a “double dome” cored by a steep vertical zone (Figs. 5b, 6a). In nature, double domes of foliation have been described in the high-grade (gneiss,

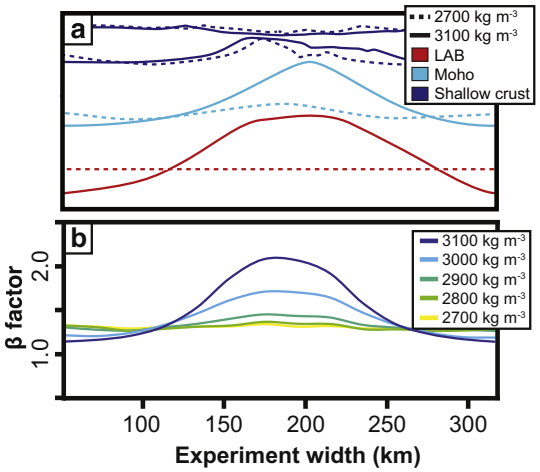

Fig. 7. (a) Lithological boundaries for a strong deep crust and two deep crust densities (28% extension). (b) Horizontal β factor profile with a strong deep crust and range of deep crust density (28% extension). Please see text for the explanation of why a denser lower crust records a higher β factor.

migmatite) cores of metamorphic core complexes (Rey et al., 2011). These are comprised of a steep high-strain zone flanked by subdomes that have experienced complex flow, including horizontal flow at upper structural levels (Kruckenberg and Whitney, 2011; Rey et al., 2011, 2017; Whitney et al., 2013).

As a result of efficient vertical mass transport, Mode A domes yield the highest exhumation velocities in the fast-extension parameter space (Fig. 5a), and are characterized by tens of kilometers of vertical transport of deep crust (Fig. 5d). These experiments therefore predict that the formation of double domes in nature involves the exhumation of high-pressure rocks to shallow crustal depths. For example, a north-south cross-section through the east-west elongated Montagne Noire double dome of the southern French Massif Central (Rey et al., 2011) resembles the cross sections of our low- and intermediate viscosity experiments (Figs. 2b$_2$, 3b$_3$, 6b). This double-dome contains eclogite that records maximum P-T conditions of ~1.4 GPa at 725 °C, corresponding to a depth of > 40 km in the orogenic crust. These eclogite units were exhumed shortly after their crystallization in the eclogite facies, during a single exhumation event along with host migmatite and granite that record crystallization at low-pressure conditions (≤ 10 km) (Whitney et al., 2015).

6. Conclusions

Results of 2D numerical experiments show that during fast extension (2 cm yr^{-1}) of the lithosphere, the viscosity and density of the deep crust exerts a first-order influence on the magnitude of exhumation experienced by rocks exposed in the core of extensional gneiss domes. Across the range of viscosity-density values in this study, under no set of conditions is the upward flow of the deep crust completely suppressed: exhumation of the deep crust occurs in every experiment. However, the mechanism and velocity of exhumation and the geometry of the extended region varies as a function of viscosity and density of the deep crust. Flow of deep crust is primarily driven by one of two mechanisms: (1) feedback between normal faulting in the upper crust and flow in the deep crust to fill the space created by the extending upper crust (for low to intermediate viscosity deep crust), creating a double-dome structure within a core complex, or (2) a passive response to relief generated on the Moho and lithosphere asthenosphere boundary during thinning of the crust and shearing of the mantle lithosphere, creating a single antiform or dome of foliation in a core complex. Slow extension (mm yr^{-1}) results in negligible exhumation of the deep crust.

Acknowledgments

The authors would like to thank an anonymous reviewer for their helpful suggestions and comments, which greatly improved the manuscript. We acknowledge John Mansour at Monash University, Australia, for generously donating his time and effort troubleshooting during Underworld installation. We also acknowledge the Minnesota Supercomputing Institute for help with software installation and management; in particular we thank Brent Schwartz, Besitie Wang, Andrew Gustafson, and Nancy Rowe for their help and advice. This research was supported by National Science Foundation (grant EAR-1050020), the Australian Research Council's ITRH Project (grant IH130200012), and the Geological Society of America (11113-15) and the Department of Earth Sciences, University of Minnesota. *Underworld* is open-source software provided by AuScope Ltd. and funded under the National Collaborative Research Infrastructure Strategy, an Australian Commonwealth Government Programme.

Appendix A. Supplementary data

Supplementary data to this article can be found online at https://doi.org/10.1016/j.tecto.2017.12.029.

References

Augier, R., Agard, P., MoniÉ, P., Jolivet, L., Robin, C., Booth-Rea, G., 2005. Exhumation, doming and slab retreat in the Betic Cordillera (SE Spain): in situ $^{40}Ar/^{39}Ar$ ages and P–T–d–t paths for the Nevado-Filabride complex. J. Metamorph. Geol. 23 (5), 357–381.

Bonev, N., Burg, J.-P., Ivanov, Z., 2005. Mesozoic–Tertiary structural evolution of an extensional gneiss dome—the Kesebir–Kardamos dome, eastern Rhodope (Bulgaria–Greece). Int. J. Earth Sci. 95 (2), 318–340.

Buck, W.R., 1991. Modes of continental lithospheric extension. J. Geophys. Res. Solid Earth 96 (B12), 20161–20178.

Burg, J.-P., Kaus, B.J.P., Podladchikov, Y.Y., 2004. Dome structures in collision orogens: Mechanical investigation of the gravity/compression interplay. Geol. Soc. Am. Spec. Pap. 380, 47–66.

Burov, E., Francois, T., Yamato, P., Wolf, S., 2014. Mechanisms of continental subduction and exhumation of HP and UHP rocks. Gondwana Res. 25 (2), 464–493.

Caby, R., Hammor, D., Delor, C., 2001. Metamorphic evolution, partial melting and Miocene exhumation of lower crust in the Edough metamorphic core complex, west Mediterranean orogen, eastern Algeria. Tectonophysics 342 (3–4), 239–273.

Clark, M.K., Royden, L.H., 2000. Topographic ooze: building the eastern margin of Tibet by lower crustal flow. Geology 28 (8), 703–706.

Clemens, J.D., Droop, G.T.R., 1998. Fluids, P–T paths and the fates of anatectic melts in the Earth's crust. Lithos 44 (1–2), 21–36.

Fayon, A.K., Whitney, D.L., Teyssier, C., 2004. Exhumation of orogenic crust: diapiric ascent versus low-angle normal faulting. In: Whitney, D.L., Teyssier, C., Siddoway, C.S. (Eds.), Gneiss Domes in Orogeny, vol. 380: Boulder, Colorado. Geological Society of America Special Paperpp. 129–139.

François, C., Philippot, P., Rey, P.F., Rubatto, D., 2014. Burial and exhumation during Archean sagduction in the East Pilbara Granite-Greenstone Terrane. Earth Planet. Sci. Lett. 396, 235–251.

Gessner, K., Wijns, C., Moresi, L., 2007. Significance of strain localization in the lower crust for structural evolution and thermal history of metamorphic core complexes. Tectonics 26 (2).

Hasterok, D., Chapman, D., 2011. Heat production and geotherms for the continental lithosphere. Earth Planet. Sci. Lett. 307 (1), 5970.

Hirth, G., Kohlstedt, D., 2004. Rheology of the upper mantle and the mantle wedge: a view from the experimentalists, inside the subduction factory. Am. Geophys. Union 83–105.

Huet, B., Le Pourhiet, L., Labrousse, L., Burov, E., Jolivet, L., 2011. Post-orogenic extension and metamorphic core complexes in a heterogeneous crust: the role of crustal layering inherited from collision. Application to the Cyclades (Aegean domain). Geophys. J. Int. 184 (2), 611–625.

Koptev, A., Burov, E., Gerya, T., Le Pourhiet, L., Leroy, S., Calais, E., Jolivet, L., 2017. Plume-induced continental rifting and break-up in ultra-slow extension context: insights from 3D numerical modeling. Tectonophysics. http://dx.doi.org/10.1016/j.tecto.2017.03.025. (in press).

Kruckenberg, S.C., Whitney, D.L., 2011. Metamorphic evolution of sapphirine- and orthoamphibole-cordierite-bearing gneiss, Okanogan dome, Washington, USA. J. Metamorph. Geol. 29 (4), 425–449.

Labrousse, L., Huet, B., Le Pourhiet, L., Jolivet, L., Burov, E., 2016. Rheological implications of extensional detachments: Mediterranean and numerical insights. Earth Sci. Rev. 161, 233–258.

Le Pourhiet, L., Huet, B., May, D.A., Labrousse, L., Jolivet, L., 2012. Kinematic interpretation of the 3D shapes of metamorphic core complexes. Geochem. Geophys. Geosyst. 13 (9).

McKenzie, D., Bickle, M.J., 1988. The volume and composition of melt generated by extension of the lithosphere. J. Petrol. 29 (3), 625–679.
Mezri, L., Le Pourhiet, L., Wolf, S., Burov, E., 2015. New parametric implementation of metamorphic reactions limited by water content, impact on exhumation along detachment faults. Lithos 236, 287–298.
Moresi, L.N., Dufour, F., Mühlhaus, H.B., 2003. A Lagrangian integration point finite element method for large deformation modelling of viscoelastic geomaterials. J. Comput. Phys. 184, 476–497.
Moresi, L., Quenette, S., Lemiale, V., Meriaux, C., Appelbe, B., Mühlhaus, H.B., 2007. Computational approaches to studying non-linear dynamics of the crust and mantle. Phys. Earth Planet. Inter. 163, 69–82.
Norlander, B.H., Whitney, D.L., Teyssier, C., Vanderhaeghe, O., 2002. Partial melting and decompression of the Thor-Odin dome, Shuswap metamorphic core complex, Canadian Cordillera. Lithos 61 (3–4), 103–125.
Paterson, M.S., Luan, F.C., 1990. Quartzite rheology under geological conditions. Geol. Soc. Lond., Spec. Publ. 54 (1), 299–307.
Rey, P.F., Muller, R.D., 2010. Fragmentation of active continental plate margins owing to the buoyancy of the mantle wedge. Nat. Geosci. 3 (4), 257–261.
Rey, P., Vanderhaeghe, O., Teyssier, C., 2001. Gravitational collapse of the continental crust: definition, regimes and modes. Tectonophysics 342 (3–4), 435–449.
Rey, P.F., Teyssier, C., Whitney, D.L., 2009a. Extension rates, crustal melting, and core complex dynamics. Geology 37 (5), 391–394.
Rey, P.F., Teyssier, C., Whitney, D.L., 2009b. The role of partial melting and extensional strain rates in the development of metamorphic core complexes. Tectonophysics 477 (3–4), 135–144.
Rey, P.F., Teyssier, C., Kruckenberg, S.C., Whitney, D.L., 2011. Viscous collision in channel explains double domes in metamorphic core complexes. Geology 39 (4), 387–390.
Rey, P.F., Mondy, L., Duclaux, G., Teyssier, C., Whitney, D.L., Bocher, M., Prigent, C., 2017. The origin of contractional structures in extensional gneiss domes. Geology 45 (3), 263–266. http://dx.doi.org/10.1130/G38595.1.
Rosenberg, C.L., Handy, M.R., 2005. Experimental deformation of partially melted granite revisited: implications for the continental crust. J. Metamorph. Geol. 23 (19–28).
Schenker, F.L., Gerya, T., Burg, J.P., 2012. Bimodal behavior of extended continental lithosphere: modeling insight and application to thermal history of migmatitic core complexes. Tectonophysics 579, 88–103.
Schulmann, K., Lexa, O., ŠTÍPskÁ, P., Racek, M., TajČManovÁ, L., KonopÁSek, J., Edel, J.B., Peschler, A., Lehmann, J., 2008. Vertical extrusion and horizontal channel flow of orogenic lower crust: key exhumation mechanisms in large hot orogens? J. Metamorph. Geol. 26 (2), 273–297.
de Sigoyer, J., Guillot, S., Dick, P., 2004. Exhumation of the ultrahigh-pressure Tso Morari unit in eastern Ladakh (NW Himalaya): a case study. Tectonics 23 (3).
Stübner, K., et al., 2013a. The giant Shakhdara migmatitic gneiss dome, Pamir, India-Asia collision zone: 2. Timing of dome formation. Tectonics 32 (5), 1404–1431.
Stübner, K., et al., 2013b. The giant Shakhdara migmatitic gneiss dome, Pamir, India-Asia collision zone: 1. Geometry and kinematics. Tectonics 32 (4), 948–979.
Teyssier, C., Whitney, D.L., 2002. Gneiss domes and orogeny. Geology 30 (12), 1139–1142.
Tirel, C., Brun, J., Burov, E., 2004a. Thermomechanical modeling of extensional gneiss domes. In: Whitney, D.L., Teyssier, C., Siddoway, C.S. (Eds.), Gneiss Domes in Orogeny, Volume 380: Boulder, Colorado. Geological Society of Americal Special Paper.
Tirel, C., Brun, J.-P., Burov, E., 2004b. Thermomechanical modeling of extensional gneiss domes. Geol. Soc. Am. Spec. Pap. 380, 67–78.
Tirel, C., Brun, J.-P., Burov, E., 2008. Dynamics and structural development of metamorphic core complexes. J. Geophys. Res. Solid Earth 113 (B4).
Toraman, E., Teyssier, C., Whitney, D.L., Fayon, A.K., Thomson, S.N., Reiners, P.W., 2014. Low-temperature thermochronologic record of Eocene migmatite dome emplacement and late Cenozoic landscape development, Shuswap core complex, British Columbia. Tectonics 33 (8), 1616–1635.
Wang, Y.F., Zhang, J.F., Jin, Z.M., Green Ii, H.W., 2012. Mafic granulite rheology: implications for a weak continental lower crust. Earth Planet. Sci. Lett. 353–354, 99–107.
Whitney, D.L., Teyssier, C., Vanderhaeghe, O., 2004. Gneiss domes and crustal flow. In: Whitney, D.L., Teyssier, C., Siddoway, C.S. (Eds.), Gneiss Domes in Orogeny, Volume 380: Boulder, Colorado. Geological Society of America Special Paperpp. 15–33.
Whitney, D.L., Teyssier, C., Rey, P., Buck, W.R., 2013. Continental and oceanic core complexes. Geol. Soc. Am. Bull. 125 (3–4), 273–298.
Whitney, D.L., Roger, F., Teyssier, C., Rey, P.F., Respaut, J.P., 2015. Syn-collapse eclogite metamorphism and exhumation of deep crust in a migmatite dome: the P–T–t record of the youngest Variscan eclogite (Montagne Noire, French Massif Central). Earth Planet. Sci. Lett. 430, 224–234.
Wijns, C., Weinberg, R., Gessner, K., Moresi, L., 2005. Mode of crustal extension determined by rheological layering. Earth Planet. Sci. Lett. 236 (1–2), 120–134.